How, where and when do radial faults grow near salt diapirs? Implications for paleo-stress analysis in sedimentary basins

Alexander J. Coleman[1], Christopher A.-L. Jackson[1], Oliver B. Duffy[2] and Maria A. Nikolinakou[2]

[1] *Basins Research Group (BRG), Department of Earth Science and Engineering, Imperial College, Prince Consort Road, London, SW7 2BP, UK.*

[2] *Bureau of Economic Geology, The University of Texas at Austin, University Station, Box X, Austin, TX 78713-7508, USA.*

**Corresponding author: a.coleman14@imperial.ac.uk*

Keywords: Salt tectonics, Radial faults, halokinetic sequences, diapirism, paleostress

ABSTRACT

We examine 3-D seismic reflection data from the Santos Basin, offshore Brazil to determine the geometry, distribution and kinematics, and to infer the origin of exceptionally well-imaged radial faults flanking and overlying a large salt stock. We propose that, during passive diapirism, radial faults nucleated at the salt-sediment interface due to circumferential extension associated with a widening salt stock. Once the stock was buried, radial faults formed in its overburden due to roof arching during punctuated active rise. The roof was then progressively shouldered aside and the faults buried along the stock flanks where they, irrespective of their origin, dip-linked with or offset one-another. We suggest that the genetic mechanism responsible for forming radial faults will

change as stocks undergo differing modes of diapirism, with our genetic mechanism likely applicable to other diapirs. Our findings not only help us to interpret the paleo-stress state of salt-bearing sedimentary basins, but also advances our understanding of fracture distributions, potential fluid flow pathways, and reservoir compartmentalization around salt diapirs in basins where seismic reflection imaging is poor.

1. INTRODUCTION

Sub-circular salt diapirs or ‘stocks’ are ubiquitous in salt-bearing sedimentary basins, and are typically associated with complex fault networks in surrounding and overlying country rock. The most common fault networks comprise ‘radial faults’ (i.e. low-displacement (<100 m) normal faults that extend radially from a salt stock into the flanking strata). Radial faults may control the migration of crustal fluids in sedimentary basins (e.g. Davison et al., 2000), and compartmentalise hydrocarbon reservoirs (e.g. Carruthers et al., 2013). In addition, radial faults record the evolving near-salt stress conditions associated with salt diapirism, with their geometry and kinematics thus helping to reconstruct paleo-stress conditions (cf. Quintà et al., 2012; Nikolinakou et al., 2014; Maerten et al., 2016).

Despite being widespread and important, the origin of radial faults in relation to specific phases of salt diapirism remains unclear. Radial faults in the unpierced roofs above rising stocks (e.g. the US Gulf Coast – Powers and Hopkins, 1922; North Sea – Carruthers et al., 2013; Basque-Pyrenees – Quintà et al., 2012) are undoubtedly related to outer-arc extension during active rise, herein termed ‘roof arching’ (Fig. 1C). Roof arching-related radial faults may nucleate anywhere in, but not necessarily extend fully across, the arched overburden. As a stock pierces its overburden, roof radial faults may be eroded or shouldered aside, and buried along the flanks of the stock (e.g. Withjack and Scheiner, 1982; Yin and Groshong Jr, 2007; Carruthers et al., 2013).

Radial faults may also form due to a widening stock pushing outwards against the flanking strata (e.g. Bishop, 1978; Nikolinakou et al., 2014), herein termed ‘stem push’ (Fig. 1D). Stem push-related radial faults form at the salt-sediment interface where circumferential stretching is greatest and where the horizontal stresses are anisotropic (i.e. $\sigma_H \neq \sigma_h$). Although numerical models suggest stem push is a plausible mechanism to form radial faults (e.g. Nikolinakou et al., 2014), this prediction has never been critically tested using observations from a natural salt diapir, nor related to a specific mode of diapirism.

The mode of diapirism is typically recorded by Composite Halokinetic Sequences or ‘CHS’ (Giles and Rowan, 2012), with two end-members recognised – tapered or tabular. Tapered CHS form during active rise, when the salt is buried by a thin roof, as sedimentation rate outpaces the volumetric flux of salt. Tabular CHS form during passive diapirism, when the salt is at or very near the surface, and the volumetric flux of salt is greater than the sedimentation rate (e.g. Giles and Rowan, 2012; Jackson and Hudec, 2017). During halokinetic active rise (in the absence of shortening), radial faults related to roof arching should form in tapered CHS. In contrast, during passive diapirism, radial faults can only form due to stem push, as there is no roof to arch. Radial faults that nucleate in tabular CHS must therefore be related to stem push.

Here, we test the hypotheses above by identifying CHS and applying quantitative fault analysis around a salt stock identified in 3-D seismic reflection data from the Santos Basin, offshore Brazil. Using this approach, we: (i) link the genetic mechanism of radial fault formation to modes of diapirism, and (ii) to the best of our knowledge, for the first time using a natural example, test the validity of the stem push model, using exceptionally well-imaged radial faults flanking and overlying a large salt stock (Fig. 2). These data not only allow us to map radial fault-diapir relationships in three-dimensions and constrain their kinematics, but also investigate when during diapirism, roof arching and stem push may occur.

Insert Fig. 1

2. DATASET AND METHODS

We used 225 km^2 of a 850 km^2, Kirchhoff pre-stack time-migrated (PSTM), zero-phase processed, 3-D seismic dataset. Inline and crossline spacing are 14 m and 25 m, respectively. A frequency of c. 15–40 Hz and assumed average velocity of c. 2000 m/s (after Jackson et al., 2014) yield an estimated vertical resolution of c. 12 m at shallow depths, decreasing to c. 35 m towards the base of supra-salt minibasins (see Appendix 1 for details). All seismic data are displayed in milliseconds two-way time (ms TWT), but measurements are converted from time to depth using an interval velocity of 2000 m/s. We mapped four seismic horizons (H1–H4) to constrain salt body geometry, and the 3-D distribution of throw on, and kinematics of, individual faults (Appendix 2). Quantitative fault analysis was not undertaken for H1 as throw was at the limit of seismic resolution (i.e. <25 m; Appendix 3). Having analysed the faults and based upon the width of folding and thinning, and the geometry (convergent or parallel) of the bounding unconformities, we then identified nine stratigraphic units adjacent to the stock that were assigned to a CHS style of Giles and Rowan (2012), thereby allowing us to interpret phases of active (tapered CHS) and passive (tabular CHS) diapiric rise (Fig. 2) (see Giles and Rowan, 2012, for recognition criteria). We then grouped the units into three packages based on CHS style and whether the stock had pierced strata at the structural level of observation. Package A consists of tabular CHS whereas packages B and C contain tapered CHS. Packages A and B have been pierced by the salt whereas Package C has not. H1 lies in Package A, H2 at the boundary between A and B, whereas H3 and H4 lie in B and C, respectively.

Insert Fig. 2

3. GEOLOGICAL SETTING

The Santos Basin formed during Early Cretaceous rifting and initial opening of the South Atlantic, during which time of a thick Aptian salt layer was deposited (the Ariri Formation) (Mohriak et al., 2008; Contreras et al., 2010). Subsequent deposition of Albian (carbonate-dominated) and Cenomanian-Holocene (siliciclastic-dominated) rocks, in addition to thin-skinned, gravity-driven extension, drove seaward salt flow and diapir growth (Demercian et al., 1993; Modica and Brush, 2004; Davison et al., 2012). We focus on a salt stock located (Fig. 1A) within the proximal, extensional domain (after Davison et al., 2012), in an area unlikely to have undergone Albian shortening. Like many diapirs in this area, the stock initiated as an extensional reactive diapir, before undergoing passive and active rise driven by sediment loading (Jackson et al., 2015). Here, we focus only on the latter stages of diapirism once the stock had developed, where CHS and radial faults are identified.

4. SALT STOCK AND OVERBURDEN GEOMETRY, AND DIAPIRISM

The salt stock is expressed in seismic data as a package of chaotic, low-amplitude reflections. In cross-section, the stock is c. 4 km tall and has a ‘teardrop’ geometry, consisting of an up to c. 4 km wide, smooth head, a <1.5 km diameter stem, and a <6 km wide pedestal (Fig. 2). The stock head overhangs the stem by c. 500 m. In plan-view, the stock is subcircular at shallow depths (c. 2000 ms TWT) and ovate at greater depths (c. 4000 ms TWT), with its long axis trending NE. The presence of tabular CHS at deeper levels indicates that, following diapir initiation, the stock entered a protracted phase of passive diapirism where the volumetric flux of salt exceeded that of the background sedimentation (Package A). Tapered CHS dominate at shallower levels, suggesting sedimentation rate outpaced the volumetric flux of salt (packages B and C). This could reflect an increase in the regional sedimentation rate, or a decreased volumetric flux of salt as the source layer thinned and ultimately welded. Based on the location of the stock in the extensional domain (after Davison et al., 2012), a lack of thrusts (cf. Withjack and Scheiner, 1982), and only minor bulb overhang (<500 m), we interpret that no shortening has taken place.

5. RADIAL FAULTS

Geometry and Distribution

Radial faults are broadly linear in map view at all stratigraphic intervals (H1–4), although they vary in their spatial distribution, density, and length (Fig. 3). They occur over a c. 2.5 km depth range (c. 1–3.5 km) within tapered and tabular CHS, although they tend to cluster around the stock head at c. 1.7 km depth (H2–4). It is possible that radial faults exist but are not imaged at greater depths (>3.5 km). Individual faults are planar, 400–1400 m tall, have aspect ratios of <2 (Appendix 4), dip at 50–60°, and have throws <80 m. Faults occur in vertically stacked tiers; faults within each tier have similar geometric characteristics e.g. heights, lengths and densities. Largely undeformed intervals define tier boundaries. Tall radial faults may cross-cut several tier boundaries and are best-developed at shallower levels around the stock's head in packages B and C (Fig. 4; Appendix 5).

Insert Fig. 3

Throw Distribution

We study the distribution of throw on radial faults to determine where these structures nucleated with respect to the stock, which in turn, may reveal the genetic mechanism responsible for their formation. Throw maxima for faults offsetting H2–4 occur immediately at or some distance from the salt-sediment interface (maximum 3 km from the stock centre; white squares on Fig. 3; Appendix 6). Faults typically have 'C-type' throw-depth profiles (*sensu* Muraoka and Kamata, 1983), with a throw maximum near their centres and very low gradients at their upper tips (<0.1) (Fig. 4A; Appendix 7). Some faults may have several throw maxima separated by throw minima, and may offset presumably older, neighbouring faults (Fig. 4B). Faults are not associated with growth strata (expansion indices of c. 1; Fig. 4), indicating the faults were blind.

Insert Fig. 4

Kinematics and Origin

Based on their geometry, stratigraphic occurrence within tapered or tabular CHS, and throw distribution, we propose the radial faults have two origins. First, we interpret that roof radial faults contained in tapered CHS with throw maxima (i.e. nucleation points; Muraoka and Kamata, 1983; Baudon and Cartwright, 2008) located both above and outboard of the stock, and which do not come in contact with the salt, reflect only roof arching (H4 in Fig. 3; Package C in Fig. 2).

Second, we interpret that radial faults in contact with the salt-sediment interface which developed in tabular CHS, formed due to stem push (H1 in Fig. 3; package A in Fig. 2), nucleating where the circumferential extension is greatest (e.g. Nikolinakou et al., 2014; Jackson and Hudec, 2017). As the stock was at or near the surface and without a roof during deposition of tabular CHS ('passive diapirism'), roof arching cannot be responsible for the formation of radial faults now deeply buried in the stock flanks. Given that the majority of deep radial faults are not physically connected to shallower roof radial faults associated with roof arching (Appendix 5), they cannot be attributed to downward propagation of the shallower faults; they must therefore reflect stem push.

In Package B, radial faults have their throw maxima either outboard of the salt or at the salt-sediment interface (H2-3 in Fig. 3). The former case suggests roof arching must have occurred; however, the latter could feasibly be explained by either: (i) stem push, or (ii) roof arching and piercement of the overburden. In the first case, radial faults nucleate where circumferential extension is greatest, due to stem push at the salt-sediment interface (Fig. 1B). In the second case, piercement of the overburden removes sections of the roof and of radial faults, altering their throw profiles. Throw maxima could therefore be only coincidentally located at the salt-sediment interface. The lack of syndepositional faulting means we are unable to identify whether stem push may have reactivated pre-existing roof arching faults as the strata became buried (e.g. Package B). Irrespective of their genetic mechanism, radial faults grew, dip-linked, and/or offset pre-existing radial faults beside the stock (Fig. 4B) (cf. Muraoka and Kamata, 1983; Baudon and Cartwright, 2008).

Integrating our CHS interpretation with quantitative fault analysis, we infer that radial fault origin is dependent on the mode of diapirism; i.e. active vs. passive rise, which at least partly reflects the balance between sedimentation rate and the volumetric flux of salt into the diapir. During passive diapirism (tabular CHS in Package A), the volumetric flux outpaced that of the background sedimentation, forming radial faults related to stem push (H1). During active rise (tapered CHS in packages B-C), sedimentation rate was greater than the volumetric flux, leading to burial of the stock and roof arching, forming radial faults in the overburden.

6. DISCUSSION AND IMPLICATIONS

Numerical (e.g. Yin and Groshong Jr, 2007) and physical (e.g. Parker and McDowell, 1951; Withjack and Scheiner, 1982) models, maps of mined salt stocks (e.g. Barton, 1925) and exposed diapirs (e.g. Powers and Hopkins, 1922; Quintà et al., 2012), and seismic reflection data (e.g. Davison et al., 2000; Stewart, 2006) permit a 2-D understanding of radial fault geometry and growth. However, by undertaking detailed mapping on 3-D seismic reflection data, we are able to not only better determine the full, 3-D geometry of *in-situ* radial fault networks, but to also constrain their kinematics. Based on our observations from the Santos Basin, we propose a genetic model that may be broadly applicable to other diapirs. We propose that, as a salt stock grows and switches between different modes of diapirism associated with changes in the volumetric flux of salt and/or sedimentation rates, it is likely the mechanism responsible for forming radial faults will change. Such changes could be due to, for example, progressive welding of supra-salt minibasins and/or changes in regional sedimentation rates.

Once passive diapirism occurs and a stock starts to grow, the volumetric flux of salt may outpace the background sedimentation rate, meaning the stock will be at or near the depositional surface. As there is no thick or persistent roof to arch at this time, stem push is the only way to form radial faults. As the source layer thins and the volumetric flux of salt decreases, a stock may become buried, with punctuated active rise driving the formation of roof arching-related radial faults in the aggrading overburden. Shouldering aside and burial of the roof along the flanks may expose these strata to stem push-related stresses, causing reactivation of existing or formation of new radial faults. Stem push-related reactivation and additional faulting is likely concentrated towards the upper parts of stocks where the greatest stress perturbations occur (e.g. Fig. 8-9 in Nikolinakou et al., 2014). Finally, as the salt supply is exhausted and minibasins weld, sedimentation rate may outpace the volumetric flux of salt, causing stock burial (cf. Giles and Rowan, 2012; Jackson and Hudec, 2017). Once diapirism ceases, no further radial faults form.

If radial faults formed by roof arching or stem push can be identified at depth, the growth history of the salt, and the tectonic history of the hosting basin can be deciphered along with the paleo-stress. As the genetic mechanism for forming radial faults likely changes during diapirism, the geometry and kinematics of those faults will likely change, especially where they have interacted to create complex fault geometries. This could prove problematic when inverting fault network geometry for paleo-stress conditions (cf. Quintà et al., 2012; Carruthers et al., 2013; Maerten et al., 2016), leading to false interpretations of stress conditions and the mode and distribution of fractures around salt stocks. For example, if radial faults due to roof arching are surface breaching (e.g. the North Sea; Carruthers et al., 2013) and are identified on the diapir flanks, then we may be able to detect episodes of halokinetic active rise that may be overlooked using tapered or tabular CHS alone. This is particularly important where near-salt imaging is poor, as is the case in many salt basins, and CHS cannot be identified.

In light of our results, we suggest that radial fault networks in other salt basins (e.g. the North Sea - Davison et al., 2000; Basque-Pyrenees – Quinta et al., 2012; US Gulf Coast – Parker and McDowell, 1951) likely reflect changes in the mode of diapirism. In addition, we highlight the structural variability and potential reservoir compartmentalisation that may occur around salt stocks, providing insights into areas where radial faults are not exposed or are poorly imaged.

ACKNOWLEDGMENTS

We thank Investigação Petrolífera Limitada (PGS) for the provision of and permission to publish seismic, Schlumberger for the provision of the Petrel software licenses to Imperial College London. Michael R. Hudec, Mahdi Heidari, Thilo Wrona and Tim P. Dooley are thanked for their discussions regarding salt-related active rise and faulting.

REFERENCES

Barton, D. C., 1925, The American salt-dome problems in the light of the Roumanian and German salt domes: AAPG Bulletin, v. 9, no. 9, p. 1227-1268.

Baudon, C., and Cartwright, J. A., 2008, 3D seismic characterisation of an array of blind normal faults in the Levant Basin, Eastern Mediterranean: Journal of Structural Geology, v. 30, no. 6, p. 746-760.

Carruthers, D., Cartwright, J., Jackson, M. P. A., and Schutjens, P., 2013, Origin and timing of layer-bound radial faulting around North Sea salt stocks: New insights into the evolving stress state around rising diapirs: Marine and Petroleum Geology, v. 48, p. 130-148.

Contreras, J., Zühlke, R., Bowman, S., and Bechstädt, T., 2010, Seismic stratigraphy and subsidence analysis of the southern Brazilian margin (Campos, Santos and Pelotas basins): Marine and Petroleum Geology, v. 27, no. 9, p. 1952-1980.

Davison, I., Alsop, G. I., Evans, N. G., and Safaricz, M., 2000, Overburden deformation patterns and mechanisms of salt diapir penetration in the Central Graben, North Sea: Marine and Petroleum Geology, v. 17, no. 5, p. 601-618.

Davison, I., Anderson, L., and Nuttall, P., 2012, Salt deposition, loading and gravity drainage in the Campos and Santos salt basins: Geological Society, London, Special Publications, v. 363, no. 1, p. 159-174.

Demercian, S., Szatmari, P., and Cobbold, P. R., 1993, Style and pattern of salt diapirs due to thin-skinned gravitational gliding, Campos and Santos basins, offshore Brazil: Tectonophysics, v. 228, no. 3, p. 393-433.

Giles, K. A., and Rowan, M. G., 2012, Concepts in halokinetic-sequence deformation and stratigraphy: Geological Society, London, Special Publications, v. 363, no. 1, p. 7-31.

Jackson, C. A.-L., Jackson, M. P., and Hudec, M. R., 2015, Understanding the kinematics of salt-bearing passive margins: A critical test of competing hypotheses for the origin of the Albian Gap, Santos Basin, offshore Brazil: Geological Society of America Bulletin, v. 127, no. 11-12, p. 1730-1751.

Jackson, C. A.-L., Jackson, M. P. A., Hudec, M. R., and Rodriguez, C., 2014, Internal structure, kinematics, and growth of a salt wall: Insights from 3-D seismic data: Geology, v. 42, no. 4, p. 307-310.

Jackson, M. P., and Hudec, M. R., 2017, Salt Tectonics: Principles and Practice, Cambridge University Press.

Maerten, L., Maerten, F., Lejri, M., and Gillespie, P., 2016, Geomechanical paleostress inversion using fracture data: Journal of Structural Geology, v. 89, p. 197-213.

Modica, C. J., and Brush, E. R., 2004, Postrift sequence stratigraphy, paleogeography, and fill history of the deep-water Santos Basin, offshore southeast Brazil: AAPG bulletin, v. 88, no. 7, p. 923-945.

Mohriak, W., Nemčok, M., and Enciso, G., 2008, South Atlantic divergent margin evolution: rift-border uplift and salt tectonics in the basins of SE Brazil: Geological Society, London, Special Publications, v. 294, no. 1, p. 365-398.

Muraoka, H., and Kamata, H., 1983, Displacement distribution along minor fault traces: Journal of Structural Geology, v. 5, no. 5, p. 483-495.

Nikolinakou, M. A., Flemings, P. B., and Hudec, M. R., 2014, Modeling stress evolution around a rising salt diapir: Marine and Petroleum Geology, v. 51, p. 230-238.

Parker, T. J., and McDowell, A. N., 1951, Scale models as guide to interpretation of salt-dome faulting: Geological notes: AAPG Bulletin, v. 35, no. 9, p. 2076-2086.

Powers, S., and Hopkins, O. B., 1922, The Brooks, Steen, and Grand Saline Salt Domes Smith and Van Zandt Counties, Texas: Washington: Government Printing Office.

Quintà, A., Tavani, S., and Roca, E., 2012, Fracture pattern analysis as a tool for constraining the interaction between regional and diapir-related stress fields: Poza de la Sal Diapir (Basque

Pyrenees, Spain): Geological Society, London, Special Publications, v. 363, no. 1, p. 521-532.

Stewart, S. A., 2006, Implications of passive salt diapir kinematics for reservoir segmentation by radial and concentric faults: Marine and Petroleum Geology, v. 23, no. 8, p. 843-853.

Withjack, M. O., and Scheiner, C., 1982, Fault patterns associated with domes--an experimental and analytical study: AAPG Bulletin, v. 66, no. 3, p. 302-316.

Yin, H., and Groshong Jr, R. H., 2007, A three-dimensional kinematic model for the deformation above an active diapir: AAPG bulletin, v. 91, no. 3, p. 343-363.

FIGURE CAPTIONS

Fig. 1 – Geographic context (A) and variance slice at 1500 ms TWT showing the 3-D seismic extent (B). Schematics for the formation of radial faults via roof arching (C) and stem push (D). The map view distribution and geometry for the radial faults with idealised throw-length plots are shown.

(column width figure)

Fig. 2 – Dip-oriented seismic section showing the plug-like salt stock and stratigraphic position of H1–4 and packages A–C. Interpreted tapered CHS – red, and tabular CHS – blue, are also shown. CHS may exhibit different degrees of upturn next to the salt, forming cusps (inset). For location, see Fig. 1B. Vertical exaggeration ~ 5. Seismic attribute is envelope.

(*column width figure*)

Fig. 3 – Variance attribute map for H1–4, delineating radial faults and the salt stock. For location, see Fig. 1B. Throw maxima (white squares) for individual radial faults and the position of Fig. 4 are also shown. No throw maxima are shown for H1, as the displacement at this level is at the limit of seismic resolution and cannot be measured accurately

(*two column width*)

Fig. 4 – Radial fault 1 and 2 throw-depth (solid line) profiles and expansion indices (dashed line). White circles and squares show the vertical fault tips and throw maxima, respectively. Radial fault 1 has a simple throw-depth profile with a single throw maxima (A). Radial fault 2 shows cross-cutting of older faults (B) and two throw maxima indicative of dip linkage. Vertical exaggeration ~ 5. H3-4 are shown. For the locations, see Fig. 3.

(two column width)

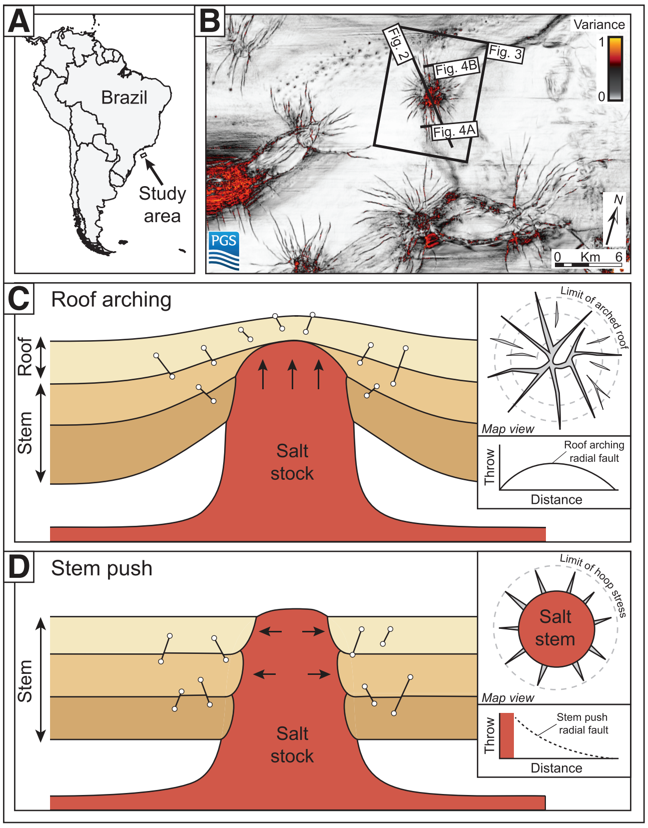
A
Brazil
Study area
B
Variance
1
0
Fig. 2
Fig. 3
Fig. 4B
Fig. 4A
PGS
N
0 Km 6
C
Roof arching
Roof
Stem
Salt stock
Limit of arched roof
Map view
Throw
Roof arching radial fault
Distance
D
Stem push
Stem
Salt stock
Limit of hoop stress
Salt stem
Map view
Throw
Stem push radial fault
Distance

Fig. 1

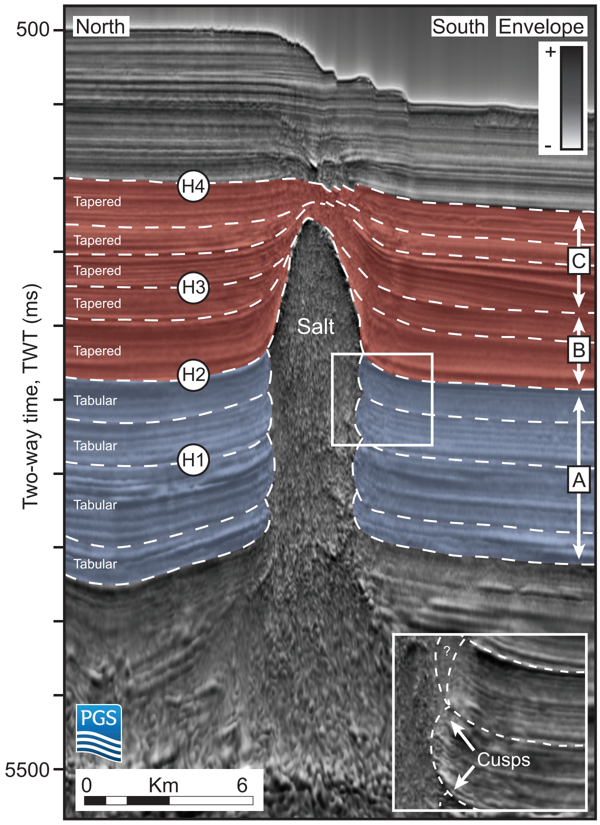

500
5500
Two-way time, TWT (ms)
North
South
Envelope
+
-
H4
Tapered
Tapered
Tapered
H3
Tapered
Tapered
H2
Tabular
Tabular
H1
Tabular
Tabular
Salt
C
B
A
?
Cusps
PGS
0
Km
6

Fig. 2

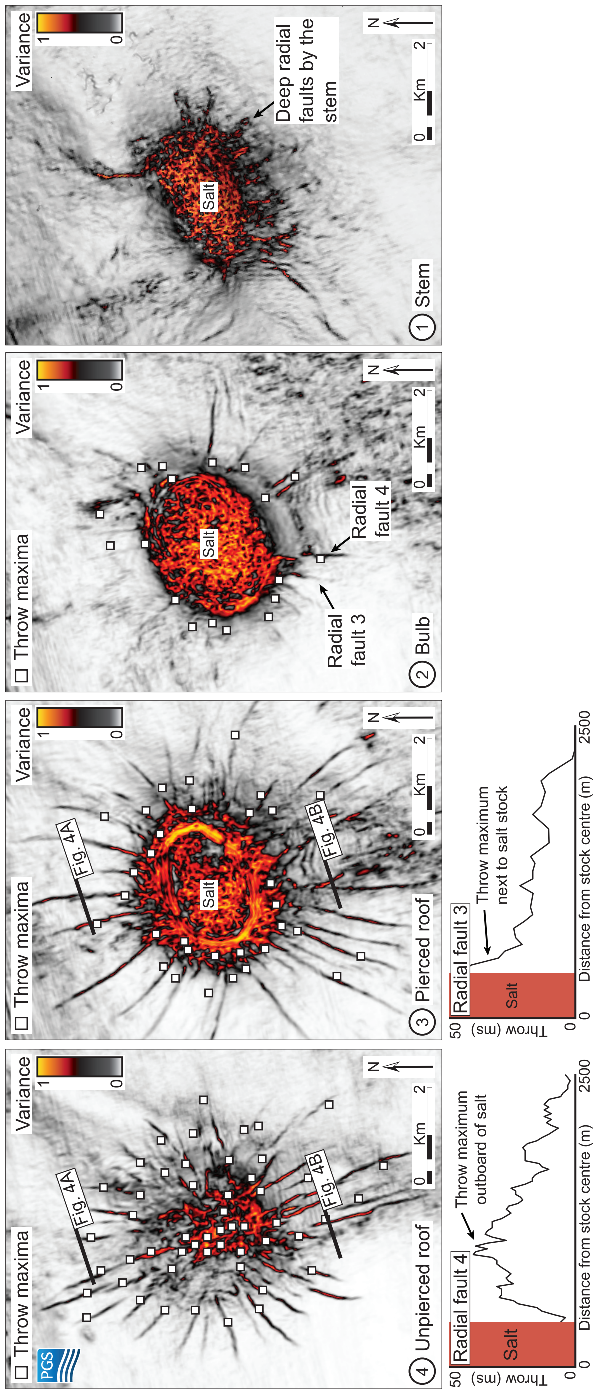
Throw maxima
Variance
1
0
PGS
Fig. 4A
Fig. 4B
Salt
0
Km
2
N
④ Unpierced roof
Radial fault 4
Salt
Throw maximum outboard of salt
50
Throw (ms)
0
0
2500
Distance from stock centre (m)
Throw maxima
Variance
Fig. 4A
Fig. 4B
Salt
③ Pierced roof
Radial fault 3
Salt
Throw maximum next to salt stock
Distance from stock centre (m)
Throw maxima
Variance
Salt
Radial fault 3
Radial fault 4
② Bulb
Variance
Salt
Deep radial faults by the stem
① Stem

Fig. 3

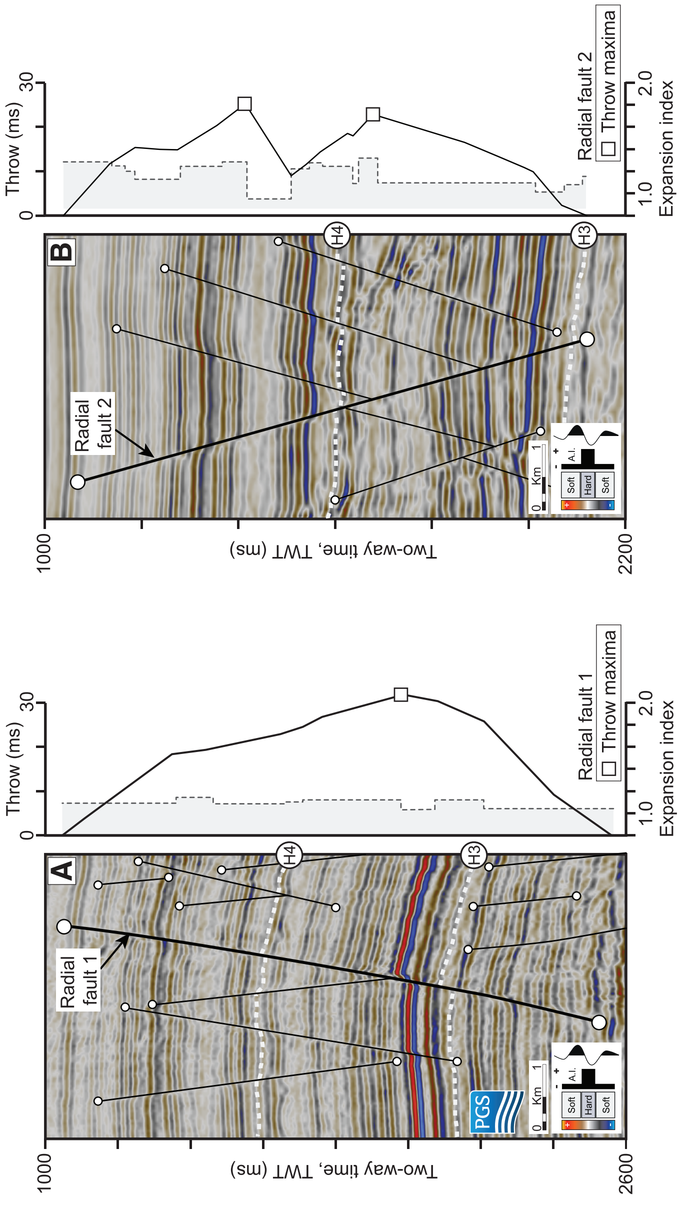
A
B
Radial fault 1
Radial fault 2
H3
H4
PGS
Two-way time, TWT (ms)
1000
2600
2200
Throw (ms)
0
30
Expansion index
1.0
2.0
Radial fault 1
Radial fault 2
Throw maxima
Km
0
1
Soft
Hard
Soft
A.I.
+
-

Fig. 4

APPENDIX 1. AVERAGE VERTICAL SEISMIC RESOLUTION

Average vertical seismic resolution (red solid line) with depth using a velocity of ~ 2 km/s (after Jackson et al., 2014) and the frequency (black dashed line). The average vertical seismic resolution was calculated using the frequency and velocity. The instantaneous frequency is shown (left).

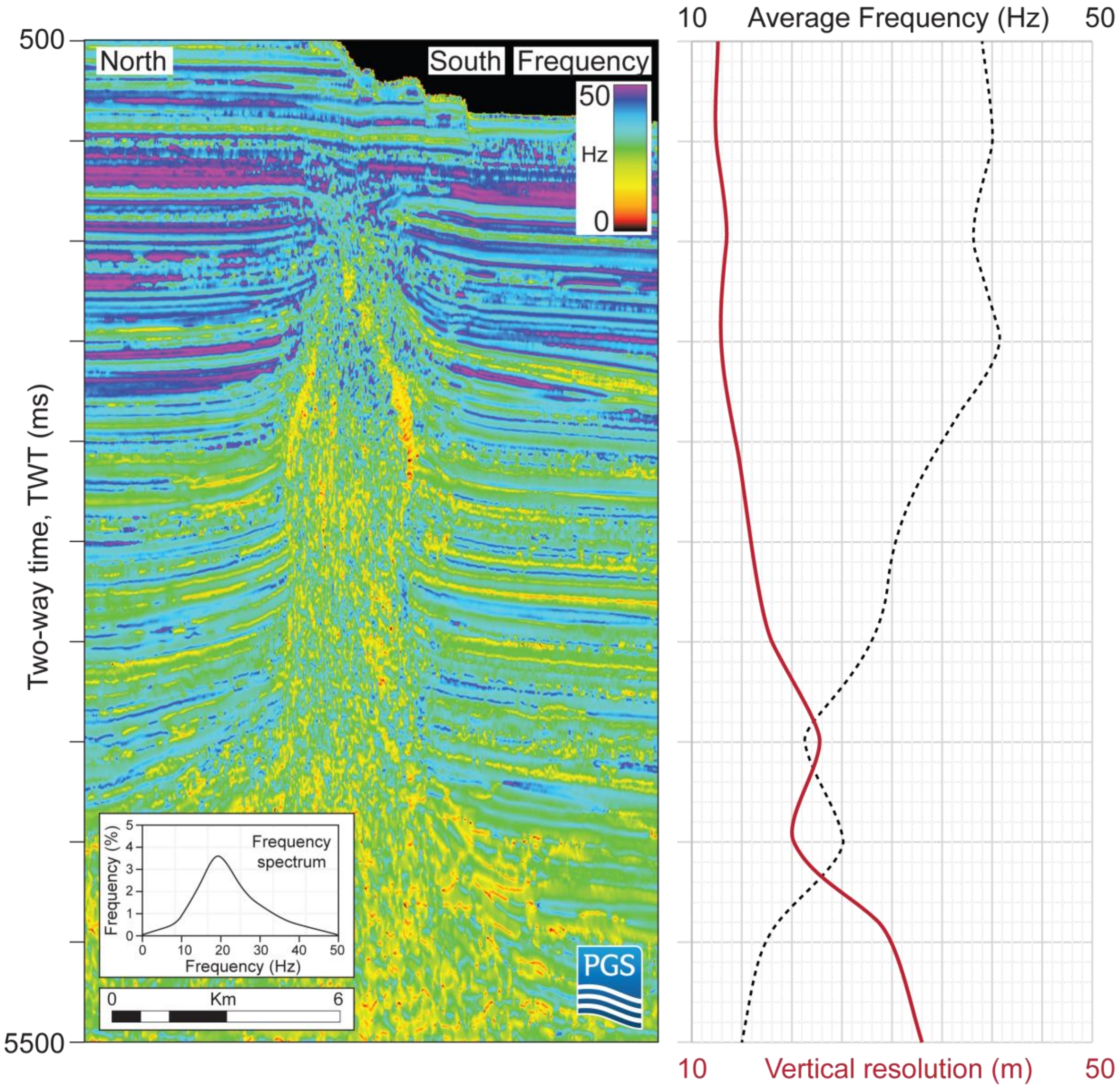

APPENDIX 2. QUANTITATIVE THROW ANALYSIS METHOD

Fault throw was measured perpendicular to radial fault strike every c. 50 – 100 m along the length of individual radial faults using horizon cut-offs (e.g. Muraoka and Kamata, 1983; Baudon and Cartwright, 2008). Cut-offs were defined using an extrapolated line that follows the regional trend of the chosen horizon prior to folding (Wilson et al., 2013), removing the effect of fault-parallel folding (Walsh et al., 1996). Therefore, total strain across the fault is accommodated, whether accommodated by ductile (continuous) or brittle (discontinuous) deformation (e.g. Long and Imber, 2010). The throw maxima was then identified on each radial fault, and plotted as white squares on Fig. 3. Fault throw was also measured with depth (T-z plots) using the aforementioned cut-offs, and throw maxima marked by white squares on Fig. 4.

Expansion indices illustrate variations in sediment thickness adjacent to fault systems, revealing the kinematics of bounding faults (e.g. Thorsen, 1963; Tvedt et al., 2013; Jackson et al., 2017). Expansion indices were calculated by dividing the hangingwall thickness of a stratal units by its corresponding footwall thickness and plotting these against geological time. An expansion index of 1 suggests no across-fault thickening, and a lack of syndepositional fault activity. An index of >1 suggests across-fault thickening and syndepositional fault activity. An index of <1 suggests stratal thinning from the footwall to the hangingwall, and may reflect difficulties in accurately measuring stratal thicknesses adjacent to a fault. Expansion indices near vertical fault tips may be slightly above and below one (± 0.1) due to ductile deformation (e.g. Barnett et al., 1987). T1 – T4 represent horizon tops. The white circle represents the vertical fault tip.

24

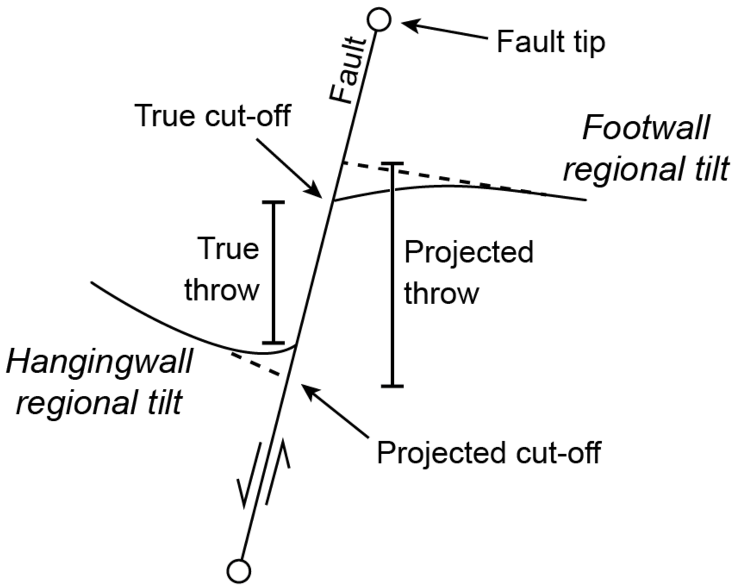
Fault tip
Fault
True cut-off
Footwall regional tilt
True throw
Projected throw
Hangingwall regional tilt
Projected cut-off

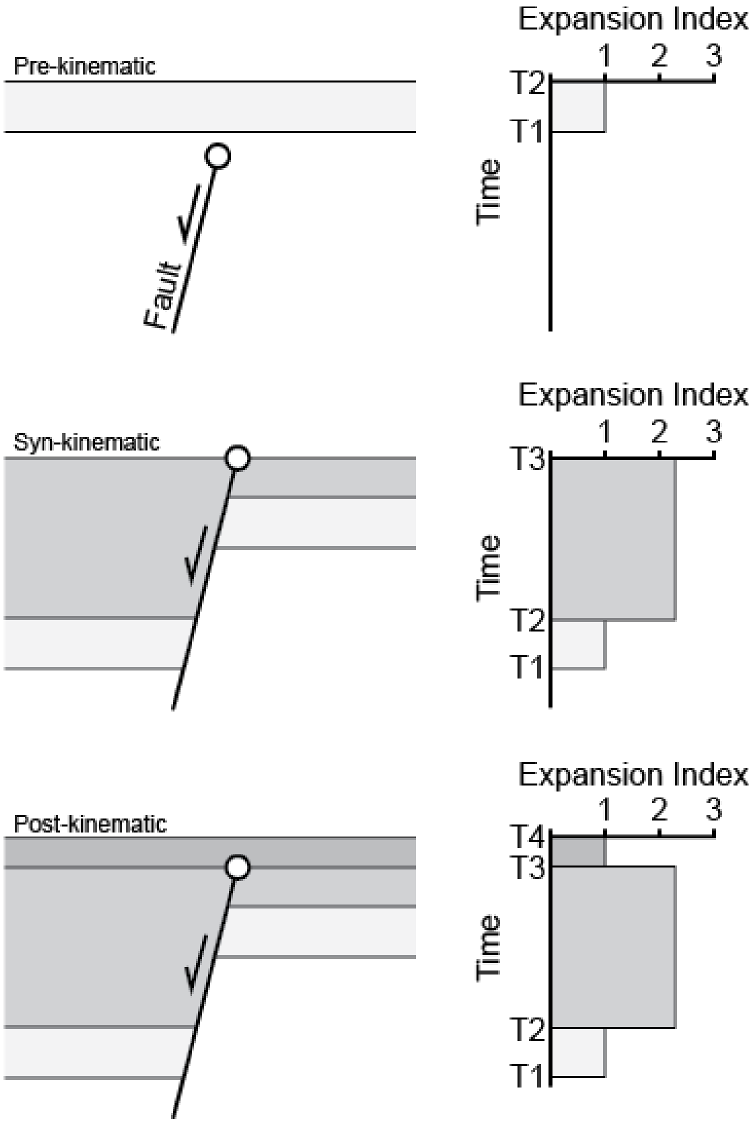
Pre-kinematic
Fault
Expansion Index
1 2 3
T2
T1
Time
Syn-kinematic
Expansion Index
1 2 3
T3
T2
T1
Time
Post-kinematic
Expansion Index
1 2 3
T4
T3
T2
T1
Time

References for Appendix 2

Barnett, J. A., Mortimer, J., Rippon, J. H., Walsh, J. J., and Watterson, J., 1987, Displacement geometry in the volume containing a single normal fault: AAPG Bulletin, v. 71, no. 8, p. 925-937.

Baudon, C., and Cartwright, J. A., 2008, 3D seismic characterisation of an array of blind normal faults in the Levant Basin, Eastern Mediterranean: Journal of Structural Geology, v. 30, no. 6, p. 746-760.

Jackson, C. A.-L., Bell, R. E., Rotevatn, A., and Tvedt, A. B. M., 2017, Techniques to determine the kinematics of synsedimentary normal faults and implications for fault growth models: Geological Society, London, Special Publications, v. 439.

Long, J., and Imber, J., 2010, Geometrically coherent continuous deformation in the volume surrounding a seismically imaged normal fault-array: Journal of Structural Geology, v. 32, no. 2, p. 222-234.

Muraoka, H., and Kamata, H., 1983, Displacement distribution along minor fault traces: Journal of Structural Geology, v. 5, no. 5, p. 483-495.

Thorsen, C. E., 1963, Age of growth faulting in southeast Louisiana.

Tvedt, A. B. M., Rotevatn, A., Jackson, C. A. L., Fossen, H., and Gawthorpe, R. L., 2013, Growth of normal faults in multilayer sequences: A 3D seismic case study from the Egersund Basin, Norwegian North Sea: Journal of Structural Geology, v. 55, p. 1-20.

Walsh, J. J., Watterson, J., Childs, C., and Nicol, A., 1996, Ductile strain effects in the analysis of seismic interpretations of normal fault systems: Geological Society, London, Special Publications, v. 99, no. 1, p. 27-40.

Wilson, P., Elliott, G. M., Gawthorpe, R. L., Jackson, C. A.-L., Michelsen, L., and Sharp, I. R., 2013, Geometry and segmentation of an evaporite-detached normal fault array: 3D seismic analysis of the southern Bremstein Fault Complex, offshore mid-Norway: Journal of Structural Geology, v. 51, p. 74-91.

APPENDIX 3. FAULT THROW RESOLUTION

Fault throw resolution for an example radial fault at Santos. Although vertical resolution may decrease with depth, the vertical offset between amplitude peaks between adjacent seismic traces permits fault throw to be measured to c. 5ms at shallow depths (< 3000 ms TWT). However, at greater depths (>3000 ms TWT), the peaks of individual traces become increasingly smeared as the vertical resolution decreases, and as such, vertical offsets are less distinct and measurement becomes increasingly difficult.

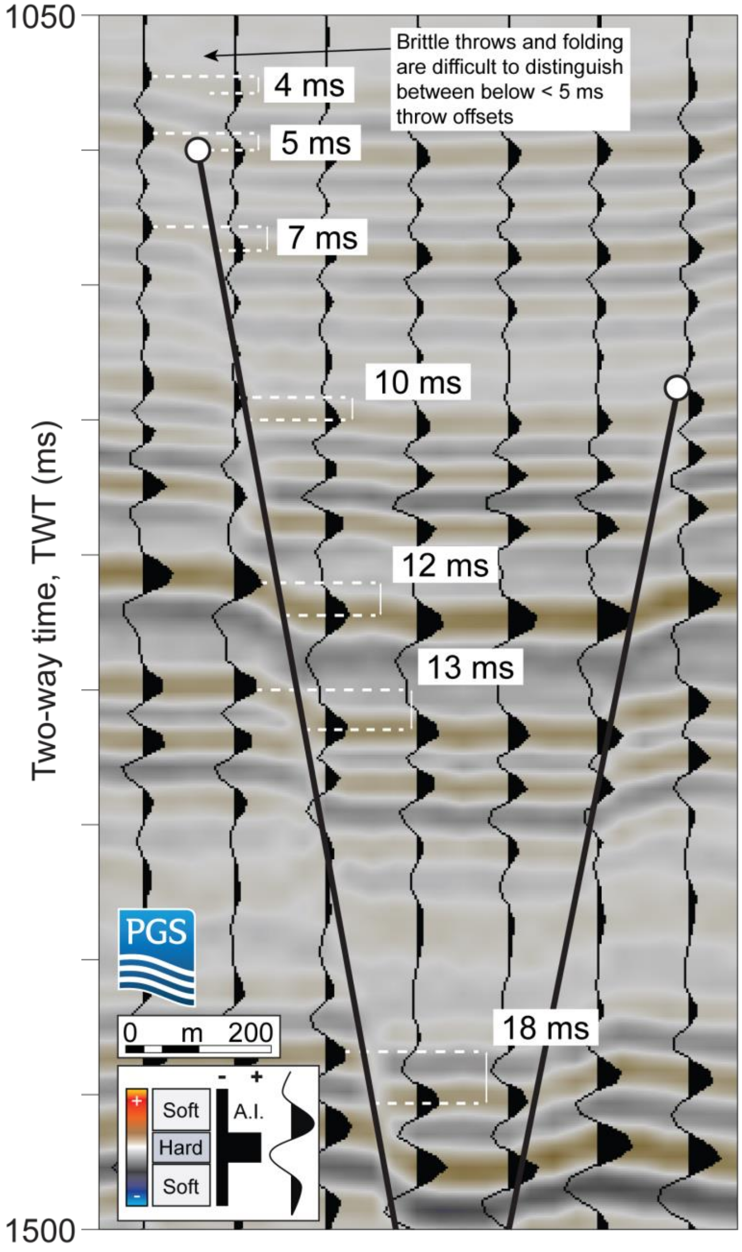

APPENDIX 4. ASPECT RATIO FOR SANTOS BASIN RADIAL FAULTS

Aspect ratios for Santos Basin radial faults. Velocity ~ 2km/s after Jackson et al. (2014).

Fault #	Max Length (m)	Height (m)	Aspect Ratio
1	3727	871	4.28
2	704	596	1.18
3	639	639	0.69
4	2021	811	2.49
5	1340	809	1.66
6	1131	655	1.73
7	601	361	1.66
8	2909	1521	1.91
9	1075	434	2.48
10	1732	650	2.66
11	644	557	1.16
12	1536	923	1.66
13	833	833	0.72
14	1542	620	2.49
15	1826	683	2.67
16	1100	208	5.29
17	1742	666	2.62
18	1322	500	2.64
19	2001	736	2.72
20	809	545	1.48
21	579	579	0.78
22	1246	275	4.53
23	1969	501	3.93
24	947	323	2.93
25	2585	676	3.82
26	882	735	1.20
27	1726	669	2.58
28	1490	731	2.04
29	1713	368	4.65
30	600	580	1.03
31	1146	663	1.73
32	644	579	1.11
33	1471	782	1.88
34	1004	350	2.87
35	412	412	0.90
36	754	496	1.52
37	903	670	1.35
38	2510	401	6.26
39	1457	693	2.10
40	464	464	0.82
41	726	726	0.52

42	540	540	0.92
43	955	685	1.39
44	856	657	1.30
45	1328	493	2.69
46	1072	734	1.46
47	791	726	1.09
48	1619	566	2.86
49	1580	551	2.87
50	1276	707	1.80
51	1288	463	2.78
52	859	701	1.23
53	1764	699	2.52
54	1090	480	2.27
55	964	596	1.62
56	754	754	0.88

APPENDIX 5. CIRCUMFERENTIAL SEISMIC SECTION

Circumferential seismic section parallel to the salt-sediment interface documenting the different vertical tiers of radial faults around the isolated salt stock. The white circles represent the vertical fault tips.

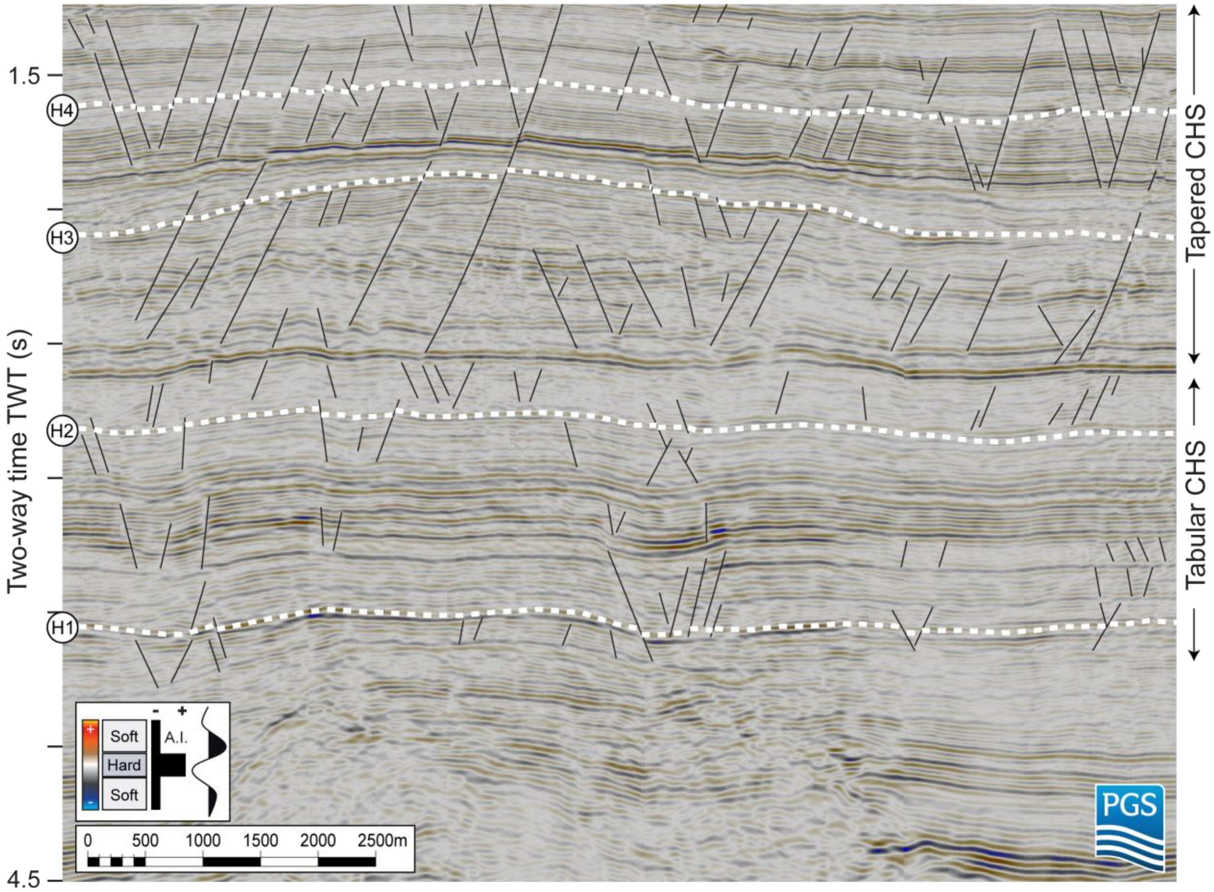

APPENDIX 6. RADIAL FAULT THROW FOR H2-4

Throw-distance on Fig. 3 used to determine the position of throw maxima along-strike for H2 - 4.

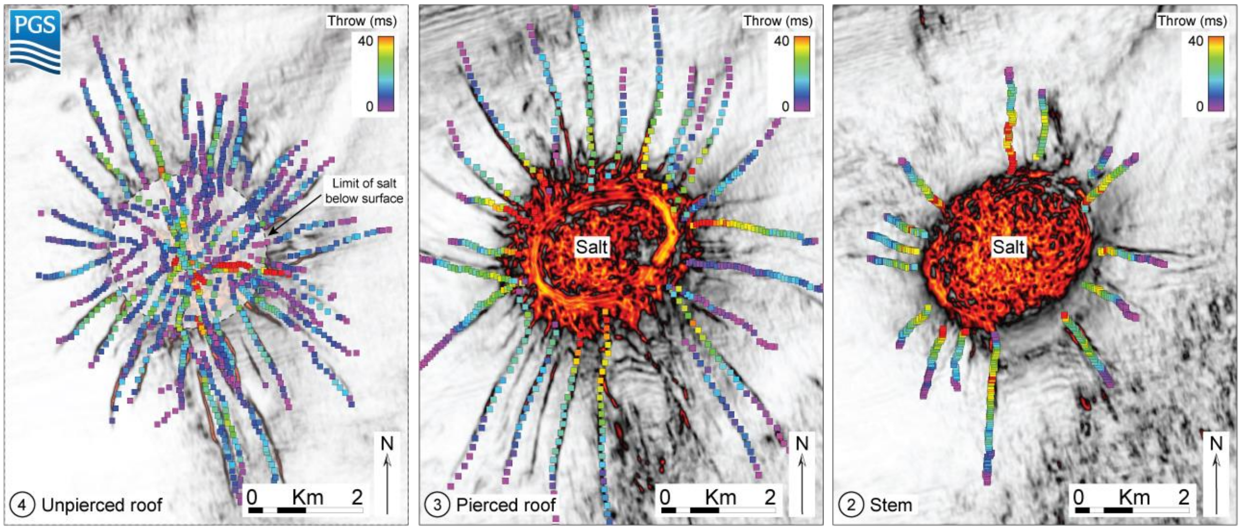

APPENDIX 7. UPPER THROW TIP GRADIENTS

Upper throw tip gradients for the Santos Basin radial faults.

Fault	Throw (m)	Upper tip radius (m)	Vertical tip throw gradient
1	47	494	0.09
2	32	308	0.10
3	25	350	0.07
4	25	281	0.09
5	25	202	0.12
6	20	139	0.14
7	26	197	0.13
8	23	499	0.05
9	23	233	0.10
10	21	303	0.07
11	36	322	0.11
12	37	507	0.07
13	21	123	0.17
14	16	151	0.11
15	15	66	0.23
16	29	254	0.11
17	38	368	0.10
18	30	307	0.10
19	24	126	0.19
20	20	338	0.06
21	20	147	0.14
22	20	305	0.07
23	20	469	0.04
24	20	454	0.04

25	66	515	0.13
26	60	499	0.12
27	22	125	0.18
28	22	206	0.11
29	23	310	0.07
30	22	427	0.05
31	21	312	0.07
32	19	231	0.08
33	19	194	0.10
34	22	396	0.06
35	24	250	0.09
36	21	335	0.06
37	14	284	0.05
38	18	247	0.07
39	21	248	0.08
40	18	337	0.05